

Effects of Pressure on Cellular Flame Structure of High Hydrogen Content Lean Premixed Syngas Spherical Flames: A DNS Study

K.K.J. Ranga Dinesh^{1*}, H. Shalaby¹, K.H. Luo², J.A. van Oijen³, D. Thévenin⁴

1. Energy Technology Research Group, Faculty of Engineering and the Environment, University of Southampton, Southampton SO17 1BJ, UK.
2. Department of Mechanical Engineering, University College London, Torrington Place, London WC1E 7JE, UK.
3. Combustion Technology Group, Department of Mechanical Engineering, Eindhoven University of Technology, Den Dolech 2, 5612 AZ Eindhoven, Netherlands.
4. Laboratory of Fluid Dynamics and Technical Flows, University of Magdeburg “Otto von Guericke”, Universitätsplatz 2, D-39106 Magdeburg, Germany.

* **Corresponding Author:** K.K.J. Ranga Dinesh, Energy Technology Research Group, Faculty of Engineering and the Environment, University of Southampton, Southampton, SO17 1BJ, UK.

Email: Dinesh.Kahanda-Koralage@soton.ac.uk

Tel: +44 (0) 2380598301

**Revised Manuscript Prepared for the Submission of International Journal of
Hydrogen Energy
September 2016**

Abstract

The structure and propagation of turbulent lean premixed high hydrogen content syngas flames at pressure values of 1bar, 2bar and 4bar are studied using three-dimensional direct numerical simulations. Simulations for each pressure considered were performed for three different initial turbulence levels at the turbulent Reynolds numbers of 50, 100 and 150. The DNS of expanding spherical flames has taken into account detailed chemical kinetics and preferential diffusion effects. The mixture-averaged transport model has been employed. Effects of pressure on flame structures, heat release rate and radical species distributions under low to high initial turbulent conditions are examined. The results show that elevated pressures greatly influence the cellular flame structure of syngas spherical flames under different initial turbulent conditions. At the atmospheric pressure, the flame shows weakly wrinkling structures due to the initial turbulence level imposed in the simulation. At elevated pressures under turbulence conditions, the flame develops cellular burning structures, superimposed by flame wrinkles due to turbulence. It is shown that highly wrinkled cells that develop over the surface of a spherical flame increase its area and thereby the global propagation speed at elevated pressures. Results show noticeable increases in the local heat release rate with increasing pressure. The analysis also reveals the formation of cusped structures with low heat release rate values in areas of negative curvatures at elevated pressures, in agreement with previous studies. The joint probability density functions of OH radical mass fraction and temperature show broadening OH values in the high temperature zone at elevated pressures compared to its distribution at the atmospheric pressure. Comparisons of mean species distributions of

OH and HO₂ over temperature between laminar and turbulent flames show that pressure elevation has a major influence on the flame structure in the composition space.

Key Words: Direct Numerical Simulation, Spherical Flames, Pressure Effects, Cellular Flame Structure, Heat Release Rate, Radicals

Introduction

Combustion engines are widely used for transportation and power generation using hydrocarbon fuels [1-4]. However, the confluence of concerns about greenhouse gas emissions and global climate change raises critical questions regarding energy sources and use [5, 6]. New strategies such as low carbon fuel options, revolutionary combustion engine designs and exhaust after-treatment systems are required to meet these challenges [7-10]. Utilisation of low carbon fuel options such as high hydrogen content (HHC) syngas fuel is important to the clean combustion technology [11-15]. In particular, burning issues of lean premixed combustion of HHC hydrogen-carbon monoxide (H_2/CO) syngas fuel at elevated pressures have received considerable attention in recent years [16-18]. For example, understanding the flame structure and propagation of highly diffusive HHC syngas fuels in lean burn mode will enable us to reduce fuel consumption and pollutant emissions.

The rapid growth in computational capabilities in the past two decades has made it possible to glean fundamental physical insights into burning characteristics of different fuels for various combustion configurations. In particular, direct numerical simulation (DNS), in which the complete spectrum of scales is resolved, is evolving as an accessible computational tool to capture fine scale turbulence-chemistry interactions and discriminate the effects of variations in fuel composition [19-25]. The premixed flame characteristics of hydrogen and hydrogen-blended hydrocarbon fuels at the atmospheric pressure have been explored by a variety of numerical experiments. For example, a number of DNS studies have examined the flame propagation speed and burning rates of

premixed and partially premixed hydrogen-air flames at the atmospheric pressure. Im and Chen [26] investigated structure and propagation speed of partially premixed hydrogen-air triple flames and compared their results with other hydrocarbon systems. Hawkes and Chen [27] studied turbulent flame speed of hydrogen blended lean premixed methane-air flames. Poludnenko and Oran [28] discussed mechanisms in determining the turbulent flame speed of hydrogen-air premixed flames in the thin reaction zone interacting with driven, subsonic, homogeneous, isotropic, Kolmogorov type turbulence in an unconfined system. Hawkes et al. [29] presented statistics for laminar flame speed and integrated burning rates and found that increased flame surface area accounts for most of the enhanced burning for hydrogen-air premixed combustion. Very recently Amato et al. [30] investigated the flame front structure at the leading edge of a turbulent lean premixed H₂-air flame, and Aspden et al. [31] discussed fuel consumption rates of turbulent lean premixed H₂-air flames. In addition, several other research questions have been addressed by DNS studies on turbulent premixed hydrogen-air combustion, which include investigation of auto-ignition of spatially non-homogenous mixtures [32] and unsteady interaction between a vortex pair and a premixed flame kernel [33], statistics of flame surface density [34], fractal characteristics and cellular structures of the flame front [35] and the interaction of turbulence with flames [36-38].

However, detailed understanding of transient flame characteristics of HHC syngas turbulent flame at elevated pressures is still lacking, particularly with respect to lean burn mode. As an effort to understand the influence of pressure on flame characteristics of HHC turbulent lean premixed H₂/CO syngas flames, a comprehensive three-dimensional

DNS study with detailed chemistry is performed in an expanding spherical flame configuration. In the context of experimental investigation of structure and propagation of turbulent premixed flames at elevated pressures, centrally-ignited outwardly propagating (expanding spherical) flame has been studied extensively [16-18, 39-44]. Experimental investigations reported the formation of cellular burning structures, cellular instabilities and burning velocities of hydrogen flames, hydrocarbon flames and syngas flames over a range of equivalence ratios and elevated pressures. In this study, we examine the influence of pressure on cellular burning structures, flame propagation and combustion intensity and radical species concentrations of the lean premixed expanding spherical flame under low to high turbulence levels initially imposed in simulations. We quantify and explain pressure effects on flame front wrinkling, local heat release rate and mass fraction of radical species distributions. The remainder of the paper is organised as follows: the governing equations, chemistry and numerical details are presented in the next section, followed by results and discussion. Conclusions and recommendations for further work are presented in the last section.

DNS Details

Mathematical Equations:

The set of governing equations solved in parallel DNS flame solver, Parcomb [45, 46] is the time-dependent compressible flow Navier-Stokes equations and chemical species transport equations. Detailed chemistry and mixture-averaged transport model are employed via coupling with the CHEMKIN [47], TRANSPORT [48] and EGLIB [49]

libraries. Using the Cartesian tensor notation and ignoring all external forces, the conservation equations solved in DNS read:

Mass conservation:

$$\frac{\partial \rho}{\partial t} + \frac{\partial(\rho u_j)}{\partial x_j} = 0 \quad (1)$$

Momentum conservation:

$$\frac{\partial(\rho u_i)}{\partial t} + \frac{\partial(\rho u_j u_i)}{\partial x_j} = -\frac{\partial p}{\partial x_i} + \frac{\partial \tau_{ij}}{\partial x_j}; \quad i = 1, 2, 3 \quad (2)$$

Species balance:

$$\frac{\partial(\rho Y_i)}{\partial t} + \frac{\partial[\rho(u_j + V_{ij})Y_i]}{\partial x_j} = \dot{\omega}_i; \quad i = 1, N_s \quad (3)$$

Energy conservation:

$$\frac{\partial(\rho e_t)}{\partial t} + \frac{\partial[(\rho e_t + p)u_j]}{\partial x_j} = -\frac{\partial q_j}{\partial x_j} + \frac{\partial(\tau_{ij}u_j)}{\partial x_i} \quad (4)$$

Equation of state:

$$\frac{p}{\rho} = \frac{R}{W} T \quad (5)$$

where t stands for time, ρ the mixture density, u_j velocity components in the x_j direction, τ_{ij} stress tensor, e_t total energy per unit mass, p pressure, Y_i the mass fraction of species i , N_s the total number of species, V_{ij} the component of the diffusion

velocity of species i in the direction j , $\dot{\omega}_i$ the chemical production rate of species i , q_j the j th-component of the heat flux vector, R the perfect gas constant ($R = 8.314 \text{ Jmol}^{-1}\text{K}^{-1}$) and \bar{W} the mixture-averaged molar mass. The H_2/CO syngas-air combustion is simulated using a skeletal mechanism developed by Goswami et al. [50, 51]. This skeletal mechanism incorporates the thermodynamic, kinetic, and species transport properties related to elevated pressure H_2 and CO oxidation, consisting of 14 species (O , O_2 , N_2 , H , H_2 , H_2O , OH , H_2O_2 , HO_2 , CO , CO_2 , HOCO , HCO , CH_2O) and 52 individual reactions.

The species diffusion velocity of species i in the mixture, V_i , is computed from the mixture-averaged transport model supplemented with Soret effect (thermal diffusion):

$$V_i = -\sum_{k=1}^{N_s} D_{ik} \mathbf{d}_k - D_i^T \frac{\nabla T}{T} \quad (6)$$

where D_{ik} denotes the multi-species diffusion coefficient matrix of species i into species k , which depends on all state variables. The mass conservation constraint for the species diffusion velocities reads $\sum_{i=1}^{N_s} Y_i V_i = 0$. \mathbf{d}_k is a species diffusion driving force vector that takes into account gradients of mole fraction and pressure. In most cases, as in the present study, the pressure-induced diffusion is negligible and the external forces \mathbf{f}_j are considered to act equally on all species, resulting simply in $\mathbf{d}_k = \nabla X_k$. D_i^T is the thermal diffusion coefficient of species i while the combined term $D_i^T \nabla T / T$ is the Soret or thermodiffusive effect, which accounts for the diffusion of mass as a result of temperature gradient. The diffusion coefficient is approximated via Hirschfelder-Curtiss approach [52]:

$$D_i^* = \frac{(1-Y_i)}{\sum_{k=1, k \neq i}^{N_s} (X_i / D_{ik})} \quad (7)$$

where D_{ik} is the binary diffusion coefficient which depends only on species pair properties, pressure and temperature and X_i is the mole fraction of species i . The diffusion velocity \mathbf{V}_i for species i is divided into a predictor (\mathbf{V}_i^*) and a corrector (\mathbf{V}_c) term in order to satisfy the mass conservation, which leads to:

$$\mathbf{V}_i = \mathbf{V}_i^* + \mathbf{V}_c; \quad \mathbf{V}_i^* = -D_i^* \frac{\nabla X_i}{X_i} - D_i^* \chi_i^* \frac{\nabla T}{T}; \quad \mathbf{V}_c = -\sum_{k=1}^{N_s} Y_k \mathbf{V}_k^* \quad (8)$$

where χ_i^* is the thermal diffusion ratio.

Several post processing equations are employed in order to analyse the detailed flame structures from the DNS data. The local heat release rate was calculated using the following formula:

$$Q = \sum_{k=1}^{N_s} h_k \dot{\omega}_k \quad (9)$$

where $\dot{\omega}_k$ ($kgm^{-3}s^{-1}$) and h_k (Jkg^{-1}) are the chemical mass production rate and species enthalpy of species k , and N_s is the total number of species involved in the oxidation processes.

To describe the local chemical state between unreacted and fully reacted mixtures, we define the non-dimensional progress variable:

$$c = \frac{T - T_u}{T_b - T_u} = \begin{cases} 0 & \text{fresh gas mixture} \\ 1 & \text{burnt gases} \end{cases} \quad (10)$$

where T_u and T_b are the unburned and burned gas temperatures, respectively.

For the purpose of evaluating strain rate and curvature effects, the tangential strain rate and curvature are also defined. Here, the tangential strain rate is given by:

$$a_T = (\delta_{ij} - N_i N_j) \frac{\partial u_i}{\partial u_j} \Big|_{c=c^*}, \quad (11)$$

where N_i is the i th component of the local flame normal vector, given by:

$$N_i = -\frac{1}{|\nabla c|} \frac{\partial c}{\partial x_i} \quad (12)$$

The local curvature was calculated from the flame front coordinates using the following formula:

$$\kappa = \frac{\partial N_i}{\partial x_i} \Big|_{c=c^*}, \quad (13)$$

where κ is taken to be positive (negative) when the flame is convex (concave) in the direction of the unburned mixture.

Flame stretch is a measure of surface deformation and defined as:

$$\mathbb{k} = \frac{1}{A} \frac{dA}{dt}, \quad (14)$$

where \mathbb{k} is the stretch, A is an element of flame area and t is time. The element of area is defined by points on the flame surface moving at the local tangential velocity and combined effects of curvature $\kappa = \nabla \cdot \mathbf{n}$ and hydrodynamic strain $K_s = -\mathbf{n} \cdot \mathbf{a}_T \cdot \mathbf{n}$, where \mathbf{a}_T is the strain rate tensor, and unit normal vector $\mathbf{n} = \nabla c / |\nabla c|$. Therefore the stretch rate

\mathbb{k} can be written as:

$$\mathbb{k} = \kappa S_d + K_s. \quad (15)$$

where S_d is the flame displacement speed.

Flame Configuration and Numerical Implementation

A series of lean premixed flames in an outwardly propagating spherical flame configuration is presented. All simulations were performed for H₂/CO syngas fuel mixture with 70% of H₂ and 30% of CO by volume, and at equivalence ratio of 0.7. The numerical configuration of a flame in a constant pressure cubic domain is shown in Fig. 1. The cubic domain has a length of 8.0×10^{-3} m on each side (Fig.1). A time step of approximately 6.0×10^{-9} s was used for all simulations. To investigate the pressure effects on flame characteristics under different turbulence levels, nine DNS test cases were performed. They were performed at three different pressure values: $p = 1$ bar, 2 bar, 4 bar, under three different initial turbulence levels with the turbulent Reynolds number, $Re_t = 50, 100, 150$, respectively. A matrix of turbulence properties and numerical parameters based on conditions at the beginning of the simulation including the turbulent Reynolds number, Damköhler number, Karlovitz number, kinematic viscosity, integral length scale, Kolmogorov length scale and total grid points in each direction, cell width, number of grid points in flame thickness, used in the present study are listed in Table 1 (a, b, c).

The equations are discretised in space on a three-dimensional Cartesian grid with high-order finite difference numerical schemes. Derivatives are computed using centered explicit schemes of order six except at boundaries where the order is progressively reduced to four. Temporal integration is realized with a Runge–Kutta algorithm of order four. A Courant-Friedrichs-Levy (CFL) condition for the convective terms and a Fourier condition pertaining to the diffusion terms are treated to ensure the stability of the explicit integration and determine a suitable time step. To maintain the constant pressure

throughout the simulation, boundary conditions are treated with the help of improved non-reflecting inflow/outflow Navier-Stokes characteristics boundary condition (NSBC) by considering additional terms in the definition of the wave amplitudes, and the relaxation treatment for the transverse gradient terms in analogy with the pressure relaxation [53]. The initial laminar spherical flame is constructed at the center of the computational domain with initial radius of $r_0 = 0.6\text{mm}$. The initial profiles of temperature and mass fractions of species is then prescribed according to:

$$\phi = \phi_0 + \frac{\Delta\phi}{2} \left[1 - \tanh \left(k \cdot \left(\frac{r - r_0}{r_0} \right) \right) \right] \quad (16)$$

Here $\Delta\phi$ is the variation between the initial approximate values in the fresh and burnt gas mixture and real number k is a measure of the stiffness at the fresh/burnt gas interface (here, $k=10.0$).

The initial isotropic turbulent velocity field for each case was initialised using a combined approach of digital filtering (DF) [54] and random noise diffusion [55]. In this approach, a linear, digital and non-recursive filter is applied to convolute a one dimensional series r_{m_x} of random data (with \bar{r}_{m_x}) such that

$$u_{m_x} = \sum_{n=-N_x}^{N_x} b_n r_{m_x+n} \quad (17)$$

where

$$b_k = \frac{\tilde{b}_k}{\left(\sum_{j=-N_x}^{N_x} \tilde{b}_j^2 \right)^{1/2}}; \quad \tilde{b}_k = \exp \left(-\frac{\pi k^2}{2n_x} \right)$$

is the filter coefficient. The preferred length scale is calculated as $l_x = n_x \Delta_x$, whereas Δ_x is the homogeneous grid spacing. The half width of the filter kernel is specified by N_x . This relation is extended to 3D by the convolution of three one-dimensional filters: $b_{ijk} = b_i b_j b_k$. A numerical error estimate

$$\max \left| \exp\left(-\frac{\pi k^2}{4n_x}\right) - \frac{\sum_{j=-N_x+k}^{N_x} b_j b_{j-k}}{\sum_{j=-N_x}^{N_x} b_j^2} \right| \leq 0.001, \quad (18)$$

for $N_x \geq 2n_x$ and $n_x = 2, \dots, 100$ is imposed on this approximately valid formulation such that the filter width should be large enough to capture twice the desired length scale l_x .

The flame thickness δ_{th} is evaluated as

$$\delta_{th} = \frac{T_b - T_u}{\max |\nabla T|}, \quad (19)$$

where T_u and T_b are the fresh and burnt gas temperatures, respectively. An initial temperature of $T_u = 300\text{K}$ is used. From the calculation of turbulence intensity u'/S_L and length-scale ratio l/δ_L , it can be concluded that the flames considered here fall mainly within the ‘‘Thin Reaction Zone (TRZ)’’ or ‘‘Thin Flamelet’’ burning regime, as shown in Fig. 2.

In the following, we perform grid sensitivity analysis for the spherical flame that develops under high turbulence and elevated pressure. We tested four different grid resolutions for the spherical flame at an elevated pressure of 4bar. The resolutions used

for four different uniform Cartesian grids are $200 \times 200 \times 200$, $400 \times 400 \times 400$, $600 \times 600 \times 600$ and $800 \times 800 \times 800$ points in x, y and z directions, respectively. The effect of grid resolution on temporal evolution of the integrated heat release rate and the spatial variation of the chemical production rate of hydrogen species is shown in Fig. 3. The comparisons of temporal evolution of the integrated heat release rate and the spatial variation of the chemical production rate of hydrogen species obtained with $200 \times 200 \times 200$ points and $400 \times 400 \times 400$ points show strong discrepancy. As seen in Fig. 3 (b), the two simulations carried out with $200 \times 200 \times 200$ points and $400 \times 400 \times 400$ points detected numerical wiggles in the spatial distribution of the chemical source term of hydrogen species. In addition, the results suggest that the temporal evolution of the integrated heat release rate shows misalignment for grids with $200 \times 200 \times 200$ and $400 \times 400 \times 400$ resolutions. However, Fig. 3 shows that a Cartesian grid with $600 \times 600 \times 600$ grid points produces grid independent results for the expanding spherical flame at pressure $p = 4$ bar and turbulent Reynolds number of $Re_t = 150$. The grid independent test performed at pressure of 4 bar provides an estimate for the required grid resolutions for the lower pressure values of $p = 1$ bar and 2 bar, respectively. Based on this estimate, we employed a Cartesian grid with $300 \times 300 \times 300$ points at a pressure value of $p = 1$ bar, and a Cartesian grid with $400 \times 400 \times 400$ points at a pressure value of $p = 2$ bar.

Results and Discussion

In discussing the DNS results we examine how pressure increment from the atmospheric to high pressures affects the cellular flame structure and flame wrinkling, the spatial variation of the heat release rate, and local variation in radical species distribution.

Cellular Flame Structure and Flame Acceleration

Fig. 4 shows instantaneous cellular burning structures of spherical flames with the influence of preferential diffusion at pressures varying from $p = 1$ bar to 4 bar under identical Re_t values (left to right), and different turbulence levels varying from $Re_t=50$ to 150 under identical pressure values (top to bottom). The instantaneous images indicate that spherical flames develop strong wrinkling structures in high pressure environment compared to atmospheric pressure. It is evident from Fig. 4 that pressure increase from $p=1$ bar to 2bar to 4bar has greatly enhanced the small scale flame wrinkling with appearance of cellular flame structures at progressively shorter unstable wavelengths. It is important to note that the development and intensity of flame wrinkling at $p=1$ bar, 2bar and 4bar under different turbulence levels is influenced by the thermo-diffusive instability via preferential diffusion, and the Darrieus-Landau hydrodynamic instability due to thermal expansion. This is the case for lean premixed high hydrogen content flames that develop under high pressure and low initial turbulence levels. However, the contribution of the thermo-diffusive instability can be overshadowed by sufficiently strong turbulence for lean premixed flames that develop under high pressures and high initial turbulence levels.

To establish a common basis for comparison of flame acceleration with respect to increasing pressure at identical Re_t values, and with respect to turbulence intensification at identical pressure values, we develop all flames to a fixed surface area of $5.685e-5 \text{ m}^2$ corresponding to isotherm of $T=620\text{K}$. The different time instants taken for expanding spherical flames to develop to a fixed surface area of $5.685e-5 \text{ m}^2$ provide two major observations: First, the expansion rate of expanding flames increases with increasing pressure under any identical Re_t conditions. For example, at $Re_t = 50$, the time taken for the expanding spherical flame to develop to a fixed surface area of $5.685e-5 \text{ m}^2$ is decreased from $t = 5.0e-4 \text{ s}$ at $p = 1 \text{ bar}$ to $t = 3.4e-4 \text{ s}$ at $p = 2 \text{ bar}$ to $t = 1.9e-4 \text{ s}$ at $p = 4 \text{ bar}$, respectively. Similar trend is also observed when pressure is increased from $p = 1 \text{ bar}$ to 2 bar to 4 bar at $Re_t = 100$ and 150 , respectively. Second, the flame also develops much faster when we increase initial turbulence level at any given pressure value. For example, when we intensify turbulence level at pressure $p = 4 \text{ bar}$, the time taken by the spherical flame to develop to a fixed surface area of $5.685e-5 \text{ m}^2$ is decreased from $t = 1.9e-4 \text{ s}$ at $Re_t=50$ to $t = 1.6e-4 \text{ s}$ at $Re_t = 100$ to $t = 1.3e-4 \text{ s}$ at $Re_t = 150$, respectively. Similar trend is also observed for flames with initial $Re_t = 50, 100$ and 150 at $p = 1 \text{ bar}$ and 2 bar , respectively. This observation suggests that the turbulent burning velocity increases with increasing pressure for turbulent flames developing under high pressure environment.

Heat Release Rate Variations and Curvature

In general, each plot in Fig. 4 demonstrates how the flame transforms into a cellular state when increasing pressure from the atmospheric to elevated values under identical initial turbulence levels. Nevertheless, it is evident from Fig. 4 that flames developing at elevated pressures display significant flame wrinkling and cellular burning structures (Fig. 4, left to right). It is known that flame wrinkling associated with increased pressure can produce positive and negative higher flame curvature values and this in turn can significantly influence the spatial variation of the unsteady heat release rate. However, Fig. 4 is restricted to temporal evolution of flame temperature. Therefore it is unclear how flame wrinkling (i.e. higher positive and negative curvature) associated with increased pressure influences the local variation of the instantaneous heat release rate. To discuss this issue, we first present the scattered data of the heat release rate versus the progress variable for each flame (Fig.5). Then we examine the spatial distribution of the heat release rate (Fig. 6), spatial distribution of curvature (Fig. 7), and scattered data of the heat release rate versus curvature along the flame front (Fig. 8).

Fig. 5 shows the scattered heat release rate data plotted versus the progress variable. There are noticeable differences between effects caused by pressure (Fig. 5, left to right) and effects caused by turbulence (Fig. 5, top to bottom) on the heat release rate. For example, the scattered data of heat release rate display less amount of scatter at $p=1\text{bar}$, and at $Re_t=50$ than at $p=2\text{bar}$, and at $Re_t=50$. Furthermore, at $p=4\text{bar}$, and at $Re_t=50$, the plot shows a significant degree of scatter in the data compared to $p=2\text{bar}$, and at $Re_t=50$. Similar behaviour is also seen when increasing pressure from 1bar to 2bar to 4bar at

$Re_t=100$ as well as $Re_t=150$. This confirms that a significant scatter in the heat release rate is caused by the stronger wrinkling and related higher positive or negative curvature effects due to increased pressure. In the meantime, Fig. 5 also shows an increasing degree of scatter at higher turbulence level compared to lower turbulence level at identical pressures. For example, at $p=1\text{bar}$, the scattered data show an increasing degree of scatter at $Re_t=100$ compared to $Re_t=50$ as well as $Re_t=150$ compared to $Re_t=100$. This confirms that the increasing amount of scatter with increasing Re_t is caused by turbulence and related higher positive and negative curvature effects. Fig. 5 also shows an increase in the maximum heat release rate with increasing pressure. For example, the maximum heat release rate at $p=1\text{bar}$ and $Re_t=50$ is $\sim 3.0 \times 10^9 \text{ Wm}^{-3}$, while its value at the elevated pressure of $p=4\text{bar}$ and $Re_t=50$ is $\sim 1.0 \times 10^{11} \text{ Wm}^{-3}$. Similarly, the peak heat release rate at $p=1\text{bar}$ and $Re_t=150$ is $\sim 4.0 \times 10^9 \text{ Wm}^{-3}$, while its value at elevated pressure value of $p=4\text{bar}$ and $Re_t=150$ is $\sim 1.4 \times 10^{11} \text{ Wm}^{-3}$. In contrast, it is noted that the increase of the maximum heat release rate with increasing turbulence level is trivial. Overall, the scattered data plots in Fig. 5 demonstrate that effects caused by pressure is more significant than effects caused by turbulence on the heat release rate of simulated flames under selected conditions.

To further elucidate the effects of pressures on unsteady heat release rate under high initial turbulence level, the spatial distribution of the heat release rate in a cross-section of the flame ball is plotted at different pressure values for $Re_t=150$ (Fig.6). As seen in Fig. 6, at $p=1\text{bar}$, the heat release rate contours show a smooth and continuous reaction zone of significant thickness. However, at $p=2\text{bar}$, the heat release rate contours show a wrinkled

reaction zone of smaller thickness compared with that at $p=1\text{bar}$. Furthermore, at $p=4\text{bar}$, the heat release rate contours demonstrate significant wrinkling and in some places discontinuous reaction zones. The overall thickness of the reaction zones at $p = 4\text{ bar}$ is much thinner than those at $p=1\text{bar}$ and 2bar , respectively. It is evident from Figs. 5 and 6 that increasing pressure increases the flame wrinkling causing higher negative (concave towards the reactants) and positive (convex towards the reactants) curvature zones [56]. We now look at iso-surfaces of the flame front coloured by local curvature and the scattered heat release rate versus curvature along the instantaneous flame front.

Fig. 7 shows iso-surfaces of flame front coloured by local curvature at pressure values of $p=1\text{bar}$, 2bar , 4bar , and at $Re_t=150$. Fig. 7 displays cells of long, medium and short wavelengths bounded by cusps (concave flame fronts) for $p=1\text{bar}$, 2bar and 4bar , respectively. It is seen that the magnitudes of both negative and positive local maximum and minimum curvature values are increasing with increasing pressure. For example, the maximum and minimum curvature values are approximately four times larger for $p=4\text{bar}$ case (8000 1/m to -8000 1/m) compared to $p=1\text{bar}$ case (2000 1/m to -2000 1/m). The formation of cusps in response to elevated pressure in our study is in agreement with the findings of Bradley and Harper [57] and Bradley [58] in high pressure spherical flame experiments. According to their observations, such cracks are prone to cross-cracking at corners, until the cracks eventually form a coherent cellular structure covering the entire flame surface, which we also observe in our DNS results at elevated pressures.

Fig. 7 further indicates that the formation of cusps structures is substantial widespread at elevated pressures in contrast to the situation observed at the atmospheric pressure. To identify the dependence of the heat release rate on positive and negative curvature zones, scatter data of the local heat release rate is plotted against the local curvature. Fig. 8 shows the scatter plot of the heat release rate versus curvature along the instantaneous flame front for each flame. It is seen that there is significantly more scatter in the heat release rate in both positive and negative curvature zones at $p=2\text{bar}$ and 4bar compared to that at $p=1\text{bar}$. Particularly, at $p=2\text{bar}$ and 4bar , more scattered data were observed in regions of higher negative curvature, where local heat release rate was generally lower. This follows from the fact that, in the higher negative curvature zone, the rate of occurrence of lower heat release rate increased indicating regions of flames close to local extinction along the flame front, as was discussed in [59]. On the other hand, increasing the turbulent Reynolds number Re_t from 10 to 150 does not have much effect on the degree of scatter in the heat release rate. It is noted that at $p = 1 \text{ bar}$ and $Re_t = 50$, the heat release rate increases with increasing positive curvature but decreases with negative curvature. However, at higher pressures or higher turbulent Reynolds numbers, such a trend is not clearly identified. Overall, the spatial distribution of the instantaneous heat release rate (Fig. 6), flame front curvature (Fig. 7), and their relationship (Fig. 8) are affected much more by elevated pressures than turbulence intensity.

Normalised Hydrogen-to-Oxygen Mass Ratio and Radical Species Mass Fractions

The objectives of this section are to evaluate the separate effects of pressure and turbulence on species distributions.

To investigate the effects of pressure at identical turbulent Reynolds number and the effects of turbulence at identical pressure, respectively, the JPDFs of temperature and normalised hydrogen-to-oxygen mass ratio are calculated. The normalised hydrogen-to-oxygen mass ratio based on the total mass fraction of element H and total mass fraction of element O is calculated using an expression:

$$\text{Local } \psi = \frac{Y_{\text{all,H}}}{2W_{\text{H}}} \bigg/ \frac{Y_{\text{all,O}}}{W_{\text{O}}}, \quad (20)$$

where $Y_{\text{all,H}}$ is the total mass fraction of element H, $Y_{\text{all,O}}$ is the total mass fraction of element O, W_{H} is the molar mass of element H and W_{O} is the molar mass of element O.

The preheat zone is defined as the region with $T < 1200\text{K}$.

As seen in Fig. 9, the JPDFs indicate the occurrence of strongest correlation at the maximum hydrogen-to-oxygen mass ratio and maximum temperature, where intense reactions take place, for all cases. A weak local peak in the JPDFs also appears at a mass ratio of about 0.4 and at a temperature of 400K in the unburnt side, which may be linked with ignition spots. The high diffusivity of hydrogen allows hydrogen to diffuse more effectively from the preheat zone to the reaction zone due to preferential diffusion effects than the oxygen molecules, resulting in a stratification of the mass ratio. Hence the mass ratio increases in the reaction zone and decreases in the unburned zone. Furthermore, for

high pressure flames, results also show slight decrease and broadening of hydrogen-to-oxygen mass ratio in the reaction zone. This could be due to increased leakage of hydrogen from the flame front due to elevated pressure. It is noted that with increasing turbulence or pressure double peaks in the JPDFs appear under identical (high) temperature ranges. Again this may be due to preferential diffusion of hydrogen.

In Fig. 10, the JPDFs of mass fraction of OH radical and temperature are shown for all cases. One observation can be made: there is strong similarity in the distribution of the JPDFs between mass fraction of OH and temperature, and those between hydrogen-to-oxygen mass ratio and temperature. The effects of pressure elevation at identical turbulent Reynolds number and the effects of turbulence intensification at identical pressure on the JPDFs between mass fraction of OH and temperature are almost identical to those on the JPDFs between normalised local hydrogen-to-oxygen mass ratio and temperature.

In Fig. 11, the JPDFs of the mass fraction of HO₂ radical species and temperature are shown. It can be seen that that the JPDFs of HO₂ mass fraction and temperature show weak correlation at lower pressure level ($p=1\text{bar}$), but strong correlation at higher pressure levels ($p = 2 \text{ bar}, 4 \text{ bar}$). At elevated pressures, the JPDFs of HO₂ and temperature show a broadening peak regions.

To further identify separate effects caused by pressure and turbulence on radical species formation, Fig. 12 shows the comparison of conditional mean values of mass fraction of

OH and HO₂ over temperature between results extracted from the simulated DNS spherical flames and the one-dimensional laminar flamelets at pressure values of 1bar, 2bar and 4bar. It is important to note that we performed one-dimensional flamelet calculations for the same conditions with the same chemistry and transport models as in DNS. Here the DNS results have been plotted for expanding spherical flames with $Re_t=150$. The conditional mean values of mass fraction of OH and HO₂ show significant changes with respect to increased pressure for turbulent spherical flames (DNS results) as well as one-dimensional laminar flames. The mass fraction of OH shows decreasing values with increasing pressure, while the mass fraction of HO₂ shows increasing values with increasing pressure. Interestingly, similar overall trend has been observed for the pressure elevation effect on the species distributions in both laminar and turbulent flames. Hence, one can argue that the pressure effects on the composition space in the turbulent and laminar flames are determined by the same reaction kinetics. Nevertheless, the mass fraction of OH shows very different distributions in the high temperature zone between the turbulent flame and the laminar flame at all three pressures. In addition, the mass fraction of HO₂ shows strong reduction of its values in the turbulent flame compared to the laminar flame while the mass fraction of OH display similar magnitude between the two flames.

Figs. 9-11 clearly demonstrate the effects of pressure elevation on key radical species such as H, OH and HO₂ for lean premixed H₂/CO combustion. This may be due to the physical effects of pressure discussed above but could also be related to the pressure-sensitive reaction mechanisms. For example, the sensitivity analysis carried out by

Goswami et al. [51] found that the reaction $\text{H}+\text{O}_2=\text{OH}+\text{O}$, and CO oxidation reaction $\text{CO}+\text{OH}=\text{CO}_2+\text{H}$ are very sensitive to changes in pressure. In addition, Goswami et al. [51] and Burke et al. [60] suggest, through flux analysis of species, that reaction $\text{H}+\text{O}_2=\text{HO}_2$ contributes significantly in the lean mixture regime, and therefore production and consumption of important radicals such as H, OH and HO_2 depend on this reaction. Goswami et al. [51] also found that in H_2/CO syngas fuel mixture, where CO is 15-30%, chemistry is subsequently dominated by H_2 , and therefore the production of carbon containing radicals such as CH_2O , HCO further helps by $\text{H}+\text{O}_2=\text{OH}+\text{O}$.

Conclusions

Three-dimensional direct numerical simulations using detailed chemistry have been presented to investigate the effects of pressure elevation on high hydrogen content lean premixed syngas spherical flames under low to high initial turbulent conditions. Simulations were performed for H_2/CO syngas fuel mixture with 70% H_2 and 30% CO by volume with an equivalence ratio of 0.7. Statistics were collected to facilitate discussions on effects of pressure on flame structure, heat release rate and species mass fraction distributions.

The main conclusions are as follows:

- a. The instantaneous temperature contours indicate that centrally-ignited turbulent spherical flames develop cellular burning structures at elevated pressures in contrast to the smooth reaction zones at the atmospheric pressure. The flame surfaces appear to be a combination of regular cellular structures and irregular wrinkles. As the pressure increases, the flame cells become smaller.

- b. It is found that the time required for the expanding turbulent spherical flame to develop to a certain surface area decreases with increasing pressure, indicating faster turbulent flame speed at elevated pressures. This is in contrast to decreased laminar flame speed as pressure increases in laminar flames.
- c. The local heat release rate shows increasing amount of scatter in both positive and negative curvature zones in flames with elevated pressures. Instantaneous heat release rate contours and scatter plots reveal the formation of cusped structures with low heat release rates at elevated pressures, which is consistent with previous findings.
- d. The joint probability density functions of hydrogen-to-oxygen mass ratio and temperature indicate flame stratification due to preferential diffusion between hydrogen and oxygen. It is found that the mass fraction of OH show qualitatively identical distribution to hydrogen-to-oxygen mass ratio. The conditional mean values of the mass fractions of radicals suggest that the pressure elevation has stronger influence on the formation of radicals such as OH and HO₂ of lean premixed H₂/CO syngas flames than turbulence. Preferential diffusion effects on the species distributions have been observed.

Acknowledgements

This work was sponsored by the Engineering and Physical Sciences Research Council (EPSRC), under the grant EP/L025051/1 (High Hydrogen Content Fuel Burning at High Pressure). Computing resources on UK National Supercomputer ARCHER funded by the EPSRC grant No. EP/J016381/2 are gratefully acknowledged.

References

1. Longwell JP, Rubin ES, Wilson J. Coal: Energy for the future. *Prog Energy Combust Sci* 1995; 21: 269-260.
2. Zhao, F, Lai MC, Harrington DL. Automotive spark-ignited direct-injection gasoline engine. *Prog Energy Combust Sci* 1999; 25: 437-562.
3. Pitz WJ, Mueller CJ. Recent progress in the development of diesel surrogate fuels. *Prog Energy Combust Sci* 2011; 37: 330-350.
4. Korakianitis T, Namasivayam AM, Crookes RJ. Natural-gas fueled spark-ignition (SI) and compression-ignition (CI) engine performance and emissions. *Prog Energy Combust Sci* 2011; 37: 89-112.
5. Sathre R. Comparing the heat of combustion of fossil fuels to the heat accumulated by their lifecycle greenhouse gases. *Fuel*; 2014: 674-677.
6. Laurmann JA. Impact of CO₂-induced climate change: strategic issues and their treatment. *Int J Hydrogen Energy* 1983; 8: 829-831.
7. Cavaliere A, de Joannon M. Mild combustion. *Prog Energy Combust Sci* 2004; 30: 329-366.
8. Al-Qurashi K, Boehman AL. Impact of exhaust gas recirculation (EGR) of the oxidative reactivity of diesel engine soot. *Combust Flame* 2008; 155: 675-695.
9. Zidansek A, Blinc R, Jeglic A, Kabashi S, Bekteshi S, Slaus I. Climate changes, biofuels and the sustainable future, *Int J Hydrogen Energy* 2009; 34: 6980-6983.
10. Yao M, Zheng Z, Liu H. Progress and recent trends in homogeneous charge compression ignition (HCCI) engines. *Prog Energy Combust Sci* 2009; 35: 398-437.

11. van Ruijven B, van Vuuren DP, de Vries B. The potential role of hydrogen in energy systems with and without climate policy. *Int J Hydrogen Energy* 2007; 32: 1655-1672.
12. Winter CJ. Hydrogen energy-Abundant, efficient, clean: A debate over the energy-system-of-change. *Int J Hydrogen Energy* 2009; 34: S1-S52.
13. Nowotny J, Veziroglu, TN. Impact of hydrogen on the environment. *Int J Hydrogen Energy* 2011; 36: 13218-13224.
14. Moriaty P, Honnery D. Hydrogen's role in an uncertain energy future. *Int J Hydrogen Energy* 2009; 34: 31-39.
15. Zerta M, Schmidt PR, Stiller C, Landinger H. Alternative world energy outlook (AWEO) and the role of hydrogen in a changing energy landscape. *Int J Hydrogen Energy* 2008; 33: 3021-3025.
16. Chiu CW, Dong YC, Shy SS. High-pressure hydrogen/carbon monoxide syngas turbulent burning velocities measured at constant turbulent Reynolds numbers. *Int J Hydrogen Energy* 2012; 37: 10935-10946.
17. Vu TM, Park J, Kwon OB, Kim JS. Effects of hydrocarbon addition on cellular instabilities in expanding syngas-air spherical premixed flames. *Int J Hydrogen Energy* 2009; 34: 6961-6969.
18. Vu TM, Park J, Kwon OB, Bae DS, Yun JH, Keel SI. Effects of diluents on cellular instabilities in outwardly propagating spherical syngas-air premixed flames. *Int J Hydrogen Energy* 2010; 35: 3868-3880.
19. Poinot T, Candel S, Trouve A. Applications of direct numerical simulation to premixed turbulent combustion. *Prog Energy Combust Sci* 1995; 21: 531-576.

20. Westbrook CK, Mizobuchi Y, Poinsoot TJ, Smith PJ, Warnatz J. Computational combustion. *Proc Combust Inst* 2005; 30: 125-157.
21. Chen JH. Petascale direct numerical simulation of turbulent combustion- fundamental insights towards predictive models. *Proc Combust Inst* 2011; 33: 99-123.
22. Ranga Dinesh KKJ, Jiang X, van Oijen JA, Bastiaans RJM, de Goey LPH. Hydrogen-enriched nonpremixed jet flames: effects of preferential diffusion. *Int J Hydrogen Energy* 2013; 38: 4848-4863.
23. Ranga Dinesh KKJ, Jiang X, van Oijen JA. Hydrogen-enriched non-premixed jet flames: compositional structures with near-wall effects. *Int J Hydrogen Energy* 2013; 38: 5150-5164.
24. Ranga Dinesh KKJ, Jiang X, van Oijen JA. Hydrogen-enriched non-premixed jet flames: analysis of the flame surface, flame normal, flame index and Wobbe index. *Int J Hydrogen Energy* 2014; 39: 6753-6763.
25. Ranga Dinesh KKJ, van Oijen JA, Luo, KH, Jiang X. Nitric oxide pollutant formation in high hydrogen content (HHC) syngas flames. *Int J Hydrogen Energy* 2015; 40: 13621-13634.
26. Im HG, Chen JH. Structure and propagation of triple flames in partially premixed hydrogen-air mixtures. *Combust Flame* 1999; 119: 436-454.
27. Hawkes ER, Chen JH. Direct numerical simulation of hydrogen-enriched lean premixed methane-air flames. *Combust Flame* 2004; 138: 242-258.
28. Poludnenko AY, Oran ES. The interaction of high-speed turbulence with flames: Turbulent flame speed. *Combust Flame* 2011; 158: 301-326.

29. Hawkes ER, Chatakonda O, Kolla H, Kerstein AR, Chen JH. A petascale direct numerical simulation study of the modelling of flame wrinkling for large-eddy simulations in intense turbulence. *Combust Flame* 2012; 159: 2690-2703.
30. Amato A, Day M, Cheng RK, Bell J, Lieuwen T. Leading edge statistics of turbulent, lean, H₂-air flames. *Proc Combust Inst* 2015; 35: 1313-1320.
31. Aspden AJ, Day MS, Bell JB. Turbulence-chemistry interaction in lean premixed hydrogen combustion. *Proc Combust Inst* 2015; 35: 1321-1329.
32. Echehki T, Chen JH. Direct numerical simulation of autoignition in non-homogeneous hydrogen-air mixtures. *Combust Flame* 2003; 134: 169-191.
33. Kolera-Gokula H, Echehki T. Direct numerical simulation of premixed flame kernel-vortex interactions in hydrogen-air mixtures. *Combust Flame* 2006; 146: 155-167.
34. Gashi S, Hult J, Jenkins KW, Chakraborty N, Cant S, Kaminski CF. Curvature and wrinkling of premixed flame kernels-comparisons of OH PLIF and DNS data. *Proc Combust Inst* 2005; 30: 809-817.
35. Shim Y, Tanaka S, Tanahashi M, Miyauchi T. Local structure and fractal characteristics of H₂-air turbulent premixed flame. *Proc Combust Inst* 2011; 33: 1455-1462.
36. Day M, Bell J, Bremer P, Pascucci V, Beckner V, Lijewski M. Turbulence effects on cellular burning structures in lean premixed hydrogen flames. *Combust Flame* 2009; 156: 1035-1045.
37. Poludnenko AY, Oran ES. The interaction of high-speed turbulence with flames: Global properties and internal flame structure. *Combust Flame* 2010; 157: 995-1011.

38. Aspden AJ, Day MS, Bell JB. Turbulence–flame interactions in lean premixed hydrogen: transition to the distributed burning regime. *J Fluid Mech* 2011; 680: 287-320.
39. Kwon OC, Rozenchan G, Law CK. Cellular instabilities and self-acceleration of outwardly propagating spherical flames. *Proc Combust Inst* 2002; 29: 1775-1783.
40. Law CK, Jomaas G, Bechtold JK. Cellular instabilities of expanding hydrogen/propane spherical flames at elevated pressures: theory and experiment. *Proc Combust Inst* 2005; 30: 159-167.
41. Wu F, Jomaas G, Law CK. An experimental investigation on self-acceleration of cellular spherical flames. *Proc Combust Inst* 2013; 34: 937-945.
42. Bradley D, Lawes M, Liu K, Verhelst S, Woolley R. Laminar burning velocities of lean hydrogen-air mixtures at pressures up to 1.0MPa. *Combust Flame* 2007; 149: 162-172
43. Bradley D, Lawes M, Liu K, Mansour MS. Measurements and correlations of turbulent burning velocities over wide ranges of fuels and elevated pressures. *Proc Combust Inst* 2013; 34: 1519-1526.
44. Askari O, Moghaddas A, Alholm A, Vien K, Alhazmi B, Metghalchi H. Laminar burning speed measurement and flame instability study of H₂/CO/air mixtures at high temperatures and pressures using a novel multi-shell model. *Combust Flame* 2016; 168: 20-31.
45. Hilbert R, Thevenin D. Autoignition of turbulent non-premixed flames investigated using direct numerical simulations. *Combust Flame* 2002; 128: 22–37.

46. Hilbert R, Tap F, El-Rabii H, Thevenin D. Impact of detailed chemistry and transport models on turbulent combustion simulations. *Prog Energy Combust Sci* 2004; 30: 165–193.
47. Kee R, Miller J, Jefferson T. Chemkin, a general purpose problem-independent transportable fortran chemical kinetics code package. Report No. SAND80-8003, Sandia National Laboratories, Livermore, CA, USA, 1980.
48. Kee R, Warnatz J, Miller J. A fortran computer code package for the evaluation of gas-phase viscosities, conductivities and diffusion coefficients. Report No. SAND83-8209, Sandia National Laboratories, Livermore, CA, USA, 1983.
49. Ern A, Giovangigli V. *eglib* server and user's manual <http://www.cmap.polytechnique.fr/www.eglib>, 2009.
50. Goswami M, Bastiaans RJM, Konnov AA, de Goey LPH. Laminar burning velocity of lean H₂-CO mixtures at elevated pressure using the heat flux method. *Int J Hydrogen Energy* 2014; 39: 1485-1498.
51. Goswami M, van Griensven JGH, Bastiaans RJM, Konnov AA, de Goey LPH. Experimental and modeling study of the effect of elevated pressure on lean high-hydrogen syngas flames. *Proc Combust Inst* 2015; 35: 655-662.
52. Hirschfelder J, Curtiss C, Bird R. *Molecular Theory of Gases and Liquids*. Wiley, New York 1954.
53. Yoo CS, Im HG. Characteristic boundary conditions for simulations of compressible reacting flows with multi-dimensional, viscous and reaction effects. *Combust Theory Model* 2007; 11: 259-286.

54. Klein M, Sadiki A, Janicka J. A digital filter based generation of inflow data for spatially developing direct numerical or large eddy simulations. *J Comput Phys* 2003; 186 : 652–665.
55. Kempf A, Klein M, Janicka J. Efficient generation of initial- and inflow-conditions for transient turbulent flows in arbitrary geometries. *Flow Turbul Combust* 2005; 74: 67–84.
56. Lee TW, North GL, Santavicca DL. Surface properties of turbulent premixed propane/air flames at various Lewis numbers. *Combust Flame* 1993; 93: 445-456.
57. Bradley D, Harper CM. The development of instabilities in laminar explosion flames. *Combust Flame* 1994; 99: 562-572.
58. Bradley D. Instabilities and flame speeds in large-scale premixed gaseous explosions . *Phil Trans R Soc Lond* 1999; A 357: 3567-3581.
59. Vena PC, Deschamps B, Guo H, Smallwood GJ, Johnson MR. Heat release rate variations in a globally stoichiometric, stratified iso-octane/air turbulent V-flame. *Combust Flame* 2015; 162: 944-959.
60. Burke MP, Chaos M, Dryer FL, Ju Y. Negative pressure dependence of mass burning rates of H₂/CO/O₂/diluent flames at low flame temperatures. *Combust Flame* 2010; 157: 618–631.

Table 1 (a, b, c): Turbulence properties and parameter ranges at three pressure values based on conditions at the beginning of the simulation.

Table 1 (a)

Case	I(a)	I(b)	I (c)
Pressure (bar)	1bar	1bar	1bar
Re_t^a	50	100	150
Da^b	0.47	0.24	0.17
Ka^c	14.99	40.35	69.92
ν (m^2/s)	1.63e-05	1.63e-05	1.63e-05
l_t (m)	6.37e-04	6.37e-04	6.37e-04
u'/S_L	2.2	4.4	6.6
l/δ_L	2.5	2.5	2.5
Grid Resolution	300×300×300	300×300×300	300×300×300
η (μm) ^d	33.9	33.9	33.9
Δx (μm)	26	26	26
Number of grid points in flame thickness	17	17	17

Table 1 (b)

Case	II (a)	II (b)	II (c)
Pressure (bar)	2bar	2bar	2bar
Re_t^a	50	100	150
Da^b	1.6	0.84	0.61
Ka^c	4.41	11.83	20.20
ν (m^2/s)	8.22e-06	8.22e-06	8.22e-06
l_t (m)	6.37e-04	6.37e-04	6.37e-04
u'/S_L	1.8	3.6	4.5
l/δ_L	5.2	5.2	5.2
Grid Resolution	400×400×400	400×400×400	400×400×400
η (μm) ^d	20.1	20.1	20.1
Δx (μm)	20	20	20
Number of grid points in flame thickness	11	11	11

Table 1 (c)

Case	II (a)	II (b)	II (c)
Pressure (bar)	4bar	4bar	4bar
Re_t^a	50	100	150
Da^b	5.71	2.99	2.17
Ka^c	1.23	3.33	5.63
ν (m ² /s)	4.13e-06	4.13e-06	4.13e-06
l_t (m)	6.37e-04	6.37e-04	6.37e-04
u'/S_L	1.6	2.1	3.2
l/δ_L	6.05	6.05	6.05
Grid Resolution	600 × 600 × 600	600 × 600 × 600	600 × 600 × 600
η (μm) ^d	14.9	14.9	14.9
Δx (μm)	13	13	13
Number of grid points in flame thickness	8	8	8

u' - Root-mean-square (RMS) turbulent fluctuation velocity

l_t -Integral length scale measured directly from the initial turbulence field

ν - Kinematic viscosity

S_L -Laminar flame speed

^aTurbulent Reynolds number, $Re_t = u' l_t / \nu$

^bDamköhler number, $Da = \left(\frac{l_t}{u'} \right) (S_L / \delta_L)$

^cKarlovitz number, $Ka = 15^{0.5} (\delta_L / S_L) (u' / \lambda)$

^dKolmogorov length scale, $\eta = l_t Re_t^{-0.75}$

λ - Taylor length scale, $\lambda = l_t Re_t^{-0.5}$

Figure Captions:

Fig.1. Configuration diagram. Expanding turbulent spherical flame at $p=2\text{bar}$ is shown.

Fig.2. Premixed combustion regime diagram with locations of current DNS test cases.

Here squares, rectangles and circles denote spherical flames at pressure of 1bar, 2bar and 4bar respectively.

Fig. 3. (a) Temporal evolution of the integrated heat release rate; (b) spatial variation of the chemical production rate of hydrogen for four different grid resolutions ($200 \times 200 \times 200$, $400 \times 400 \times 400$, $600 \times 600 \times 600$ and $800 \times 800 \times 800$) for the expanding spherical flame at turbulent Reynolds number of $Re_t=150$, and at pressure of $p=4\text{bar}$.

Fig. 4. Instantaneous snapshots of flame temperature iso-surfaces for three pressure values varying from $p=1\text{bar}$ to 4bar at identical turbulent Reynolds number (left to right), and three turbulent Reynolds numbers varying from $Re_t=50$ to 150 at identical pressure (top to bottom).

Fig. 5. Scatterplots of heat release rate for three pressure values varying from $p=1\text{bar}$ to 4bar at identical Re_t (left to right), and three turbulent Reynolds numbers varying from $Re_t=50$ to 150 at identical pressure (top to bottom).

Fig. 6. Contour plots of heat release rate (left hand side: full domain, right hand side: zoom view of the selected region) for three pressure values of $p=1\text{bar}$, 2bar and 4bar and at identical turbulent Reynolds number of $Re_t=150$. Note the different scales for the colorbar from top to bottom.

Fig. 7. Iso-surfaces of flame front ($c=0.5$), coloured by local curvature values (left hand side: full domain, right hand side: zoom view of the selected region) for three pressure

values of $p=1\text{bar}$, 2bar and 4bar and at identical turbulent Reynolds number of $Re_t=150$.

Note the different scales for the colorbar from top to bottom.

Fig.8. Scatterplots of heat release rate versus curvature at flame front for three pressure values varying from $p=1\text{bar}$ to 4bar at identical Re_t (left to right), and three turbulent Reynolds numbers varying from $Re_t=50$ to 150 at identical pressure (top to bottom).

Fig. 9. Joint probability density function of hydrogen-to-oxygen mass ratio as a function of temperature for three pressure values varying from $p=1\text{bar}$ to 4bar at identical Re_t (left to right), and three turbulent Reynolds numbers varying from $Re_t=50$ to 150 at identical pressure (top to bottom).

Fig. 10. Joint probability density function of mass fraction of OH as a function of temperature for three pressure values varying from $p=1\text{bar}$ to 4bar at identical Re_t (left to right), and three turbulent Reynolds numbers varying from $Re_t=50$ to 150 at identical pressure (top to bottom).

Fig. 11. Joint probability density function of mass fraction of HO_2 as a function of temperature for three pressure values varying from $p=1\text{bar}$ to 4bar at identical Re_t (left to right), and three turbulent Reynolds numbers varying from $Re_t=50$ to 150 at identical pressure (top to bottom).

Fig. 12. Conditional mean values of mass fractions of OH and HO_2 radicals as a function of temperature for three pressure values of $p=1\text{bar}$ to 4bar , (a) for turbulent flames with Reynolds number of $Re_t=150$ and, (b) for one-dimensional laminar flamelet.

Figures:

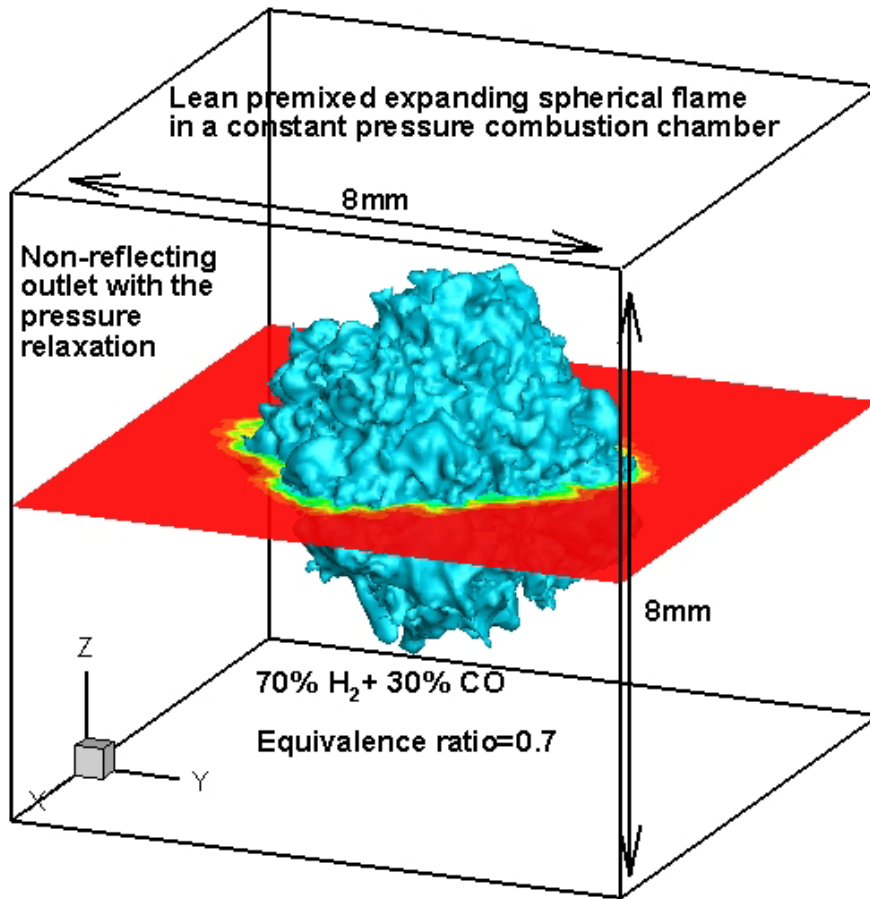


Fig.1. Configuration diagram. Expanding turbulent spherical flame at $p=2\text{bar}$ is shown.

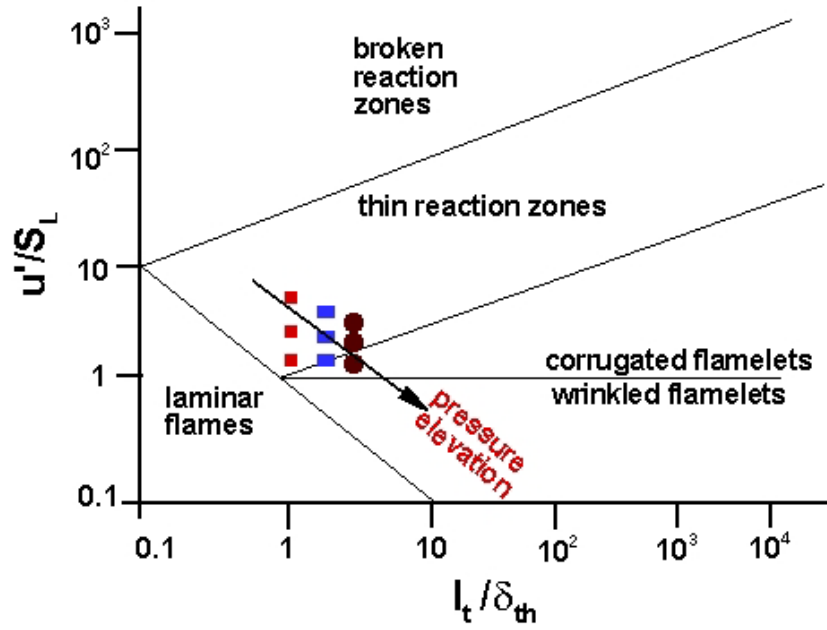
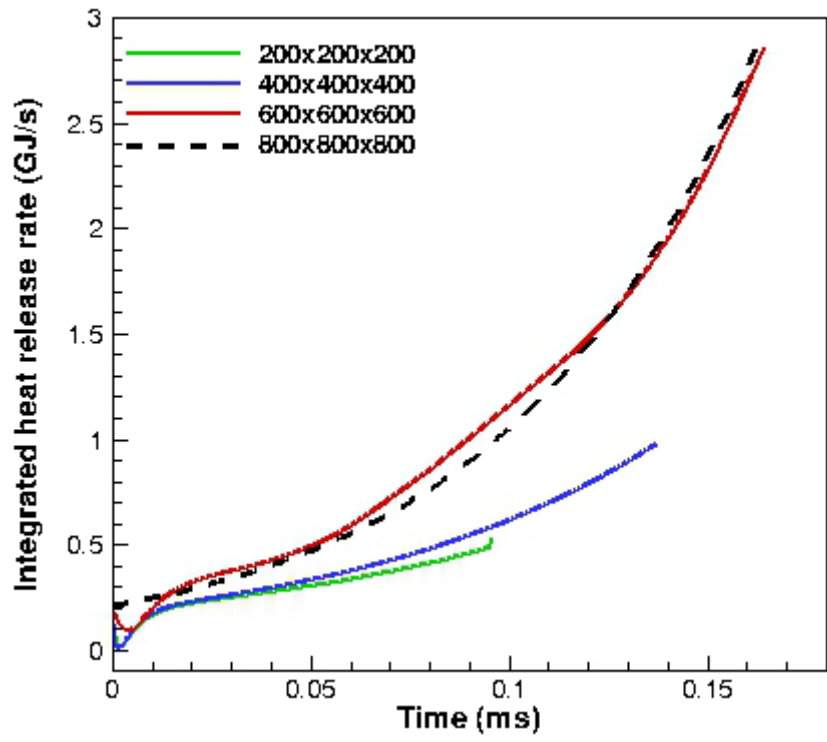
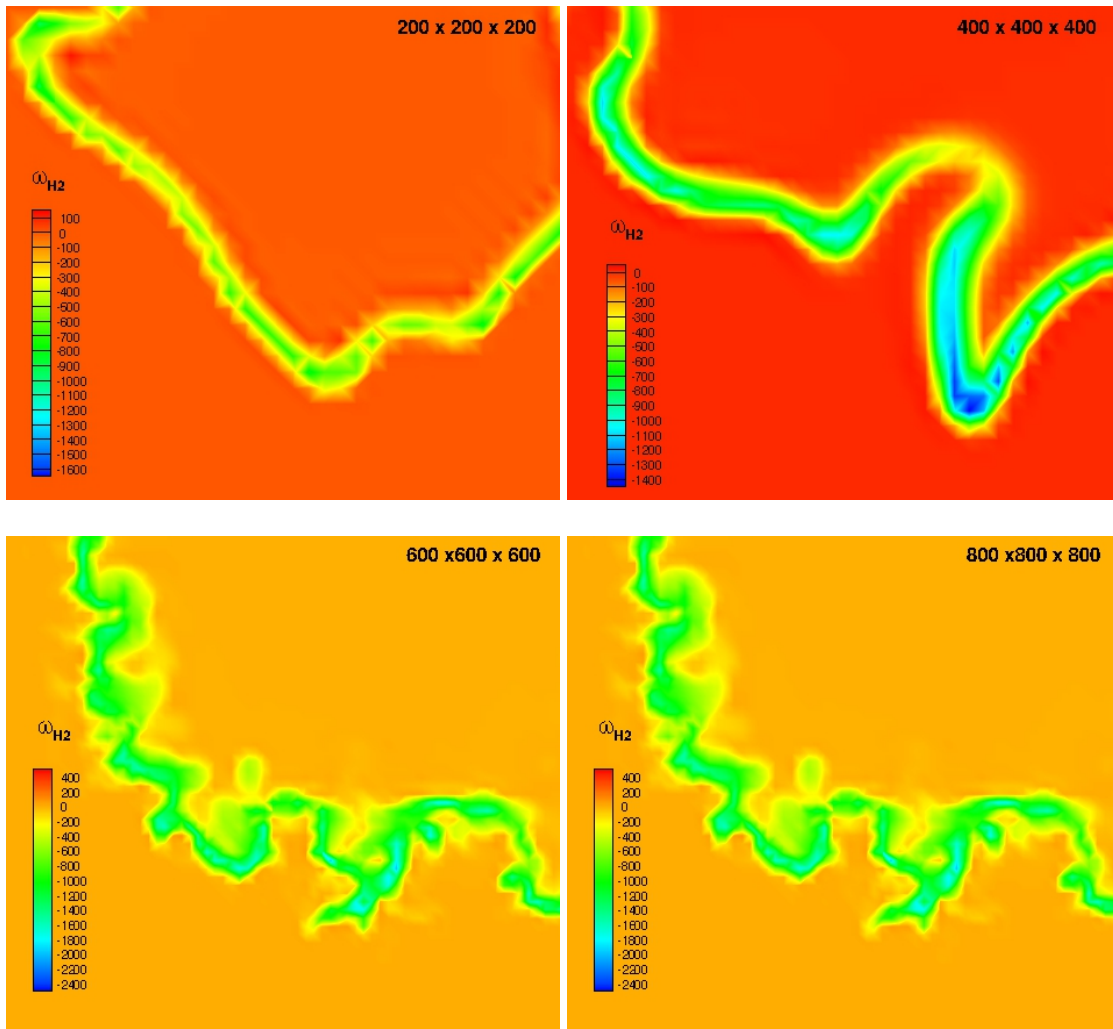


Fig.2. Premixed combustion regime diagram with locations of current DNS test cases. Here squares, rectangles and circles denote spherical flames at pressure of 1bar, 2bar and 4bar respectively.



(a)



(b)

Fig. 3. (a) Temporal evolution of the integrated heat release rate; (b) spatial variation of the chemical production rate of hydrogen for four different grid resolutions ($200 \times 200 \times 200$, $400 \times 400 \times 400$, $600 \times 600 \times 600$ and $800 \times 800 \times 800$) for the expanding spherical flame at turbulent Reynolds number of $Re_t=150$, and at pressure of $p=4\text{bar}$.

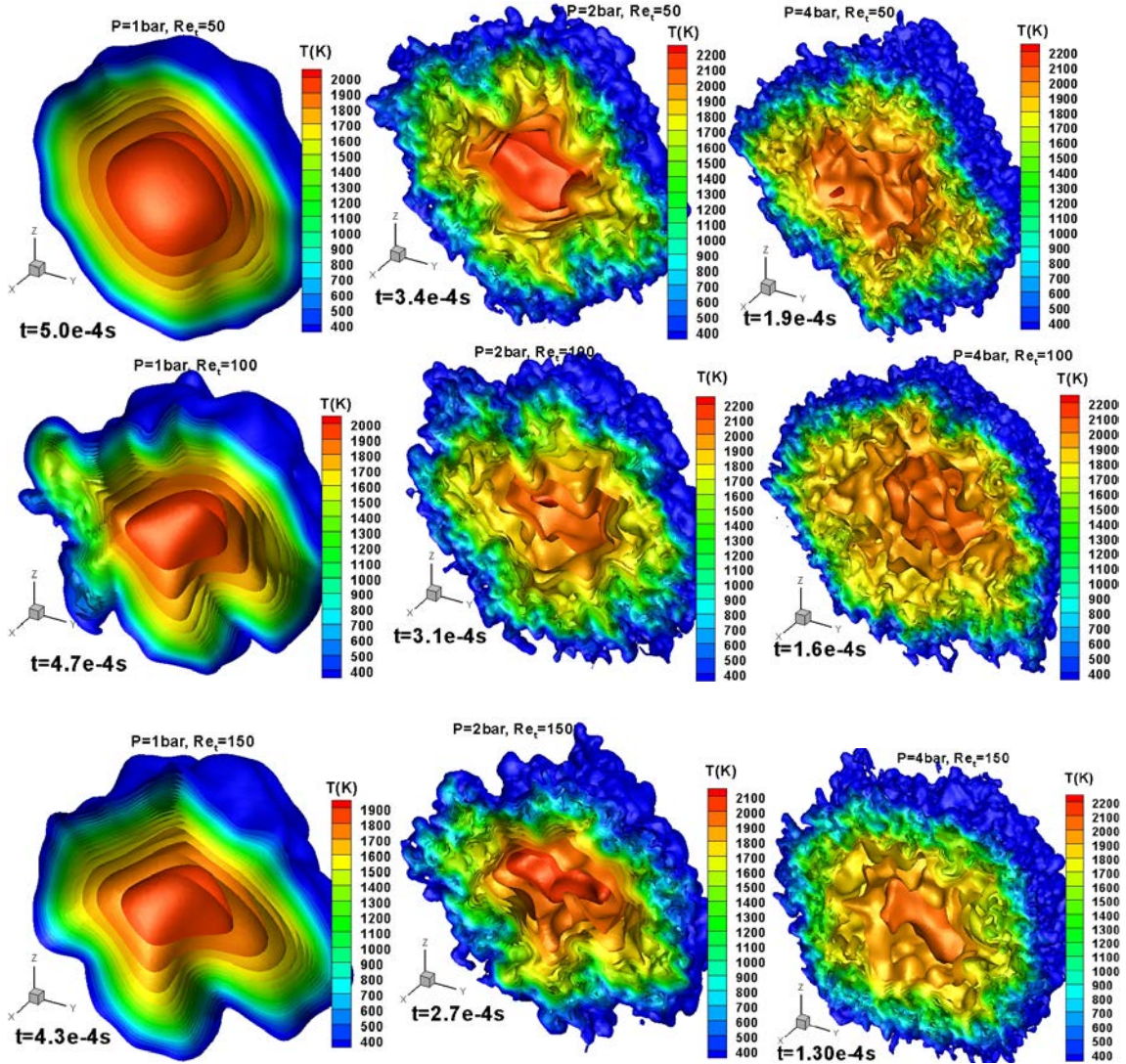


Fig. 4. Instantaneous snapshots of flame temperature iso-surfaces for three pressure values varying from $p=1\text{ bar}$ to 4 bar at identical turbulent Reynolds number (left to right), and three turbulent Reynolds numbers varying from $Re_t=50$ to 150 at identical pressure (top to bottom).

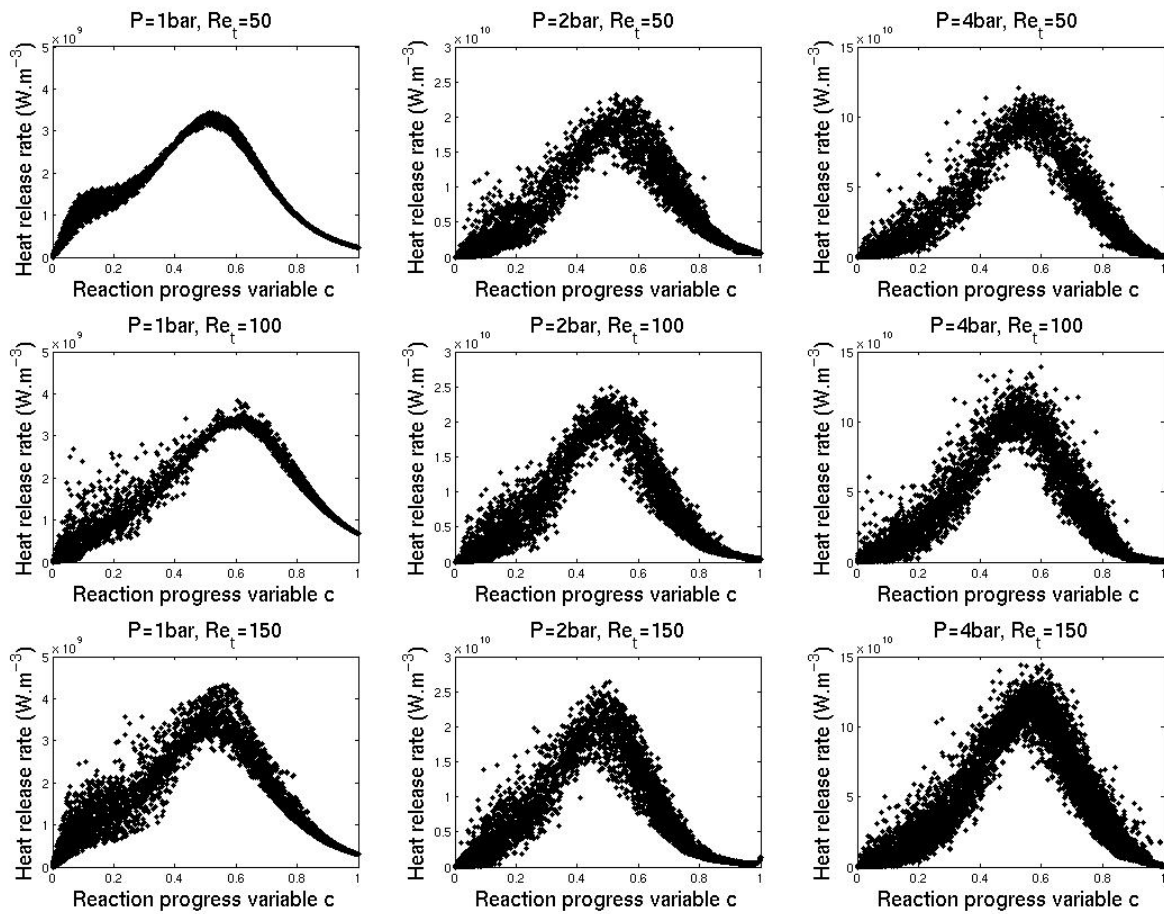


Fig. 5. Scatterplots of heat release rate for three pressure values varying from $p=1$ bar to 4 bar at identical Re_t (left to right), and three turbulent Reynolds numbers varying from $Re_t=50$ to 150 at identical pressure (top to bottom).

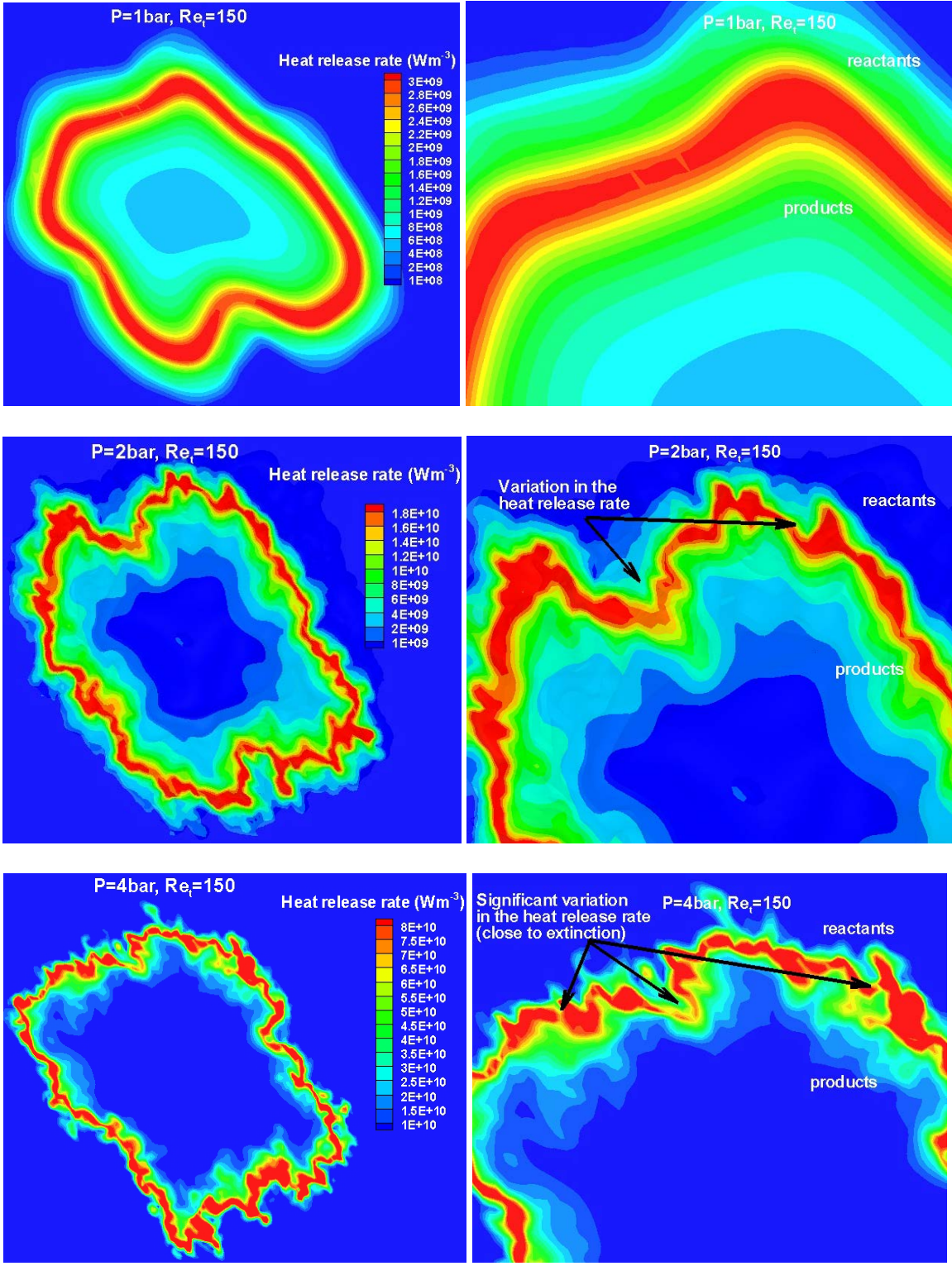


Fig. 6. Contour plots of heat release rate (left hand side: full domain, right hand side: zoom view of the selected region) for three pressure values of $p=1\text{bar}$, 2bar and 4bar and at identical turbulent Reynolds number of $Re_t=150$. Note the different scales for the colorbar from top to bottom.

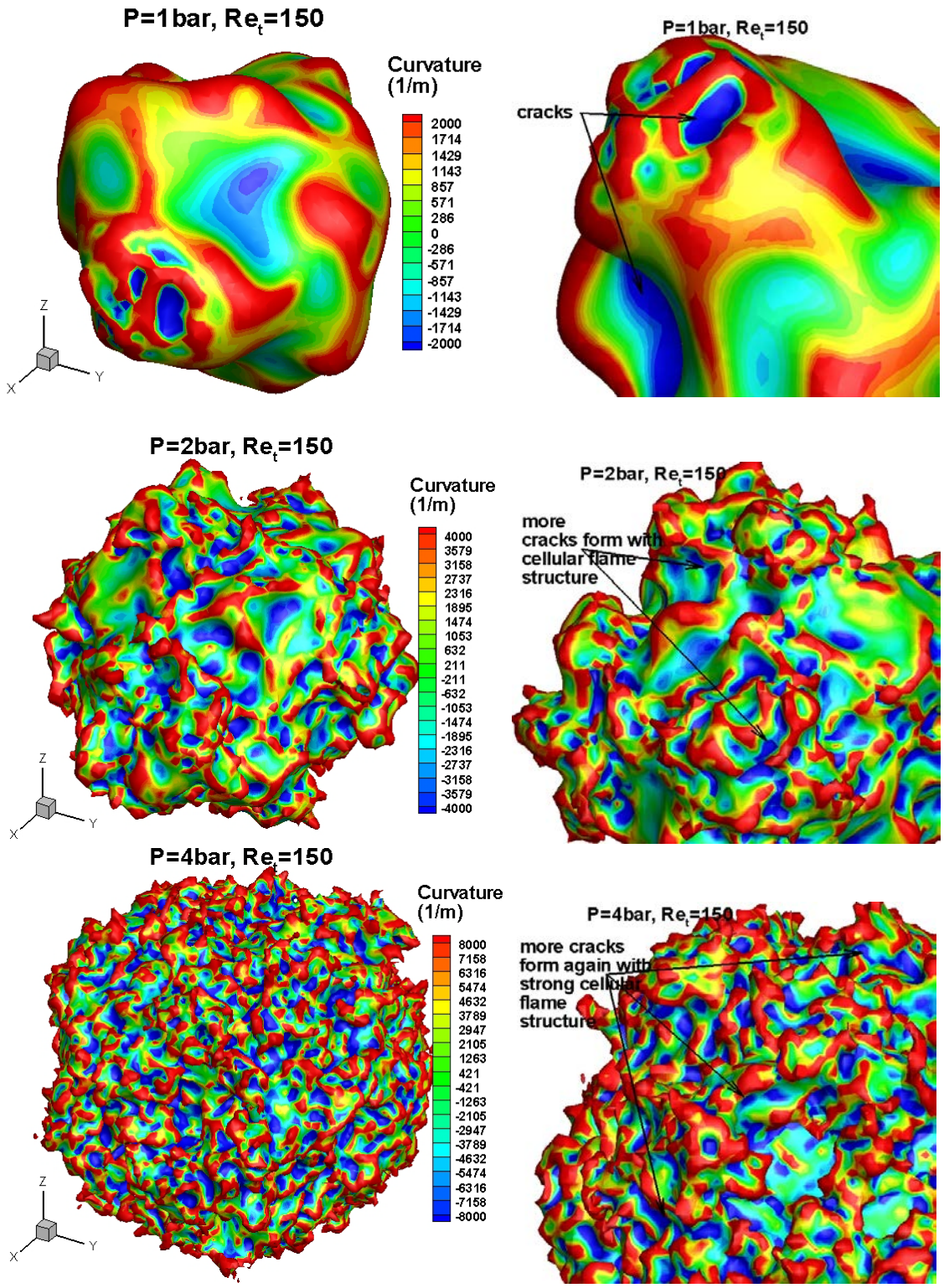


Fig. 7. Iso-surfaces of flame front ($c=0.5$), coloured by local curvature values (left hand side: full domain, right hand side: zoom view of the selected region) for three pressure values of $p=1\text{bar}$, 2bar and 4bar and at identical turbulent Reynolds number of $Re_t=150$. Note the different scales for the colorbar from top to bottom.

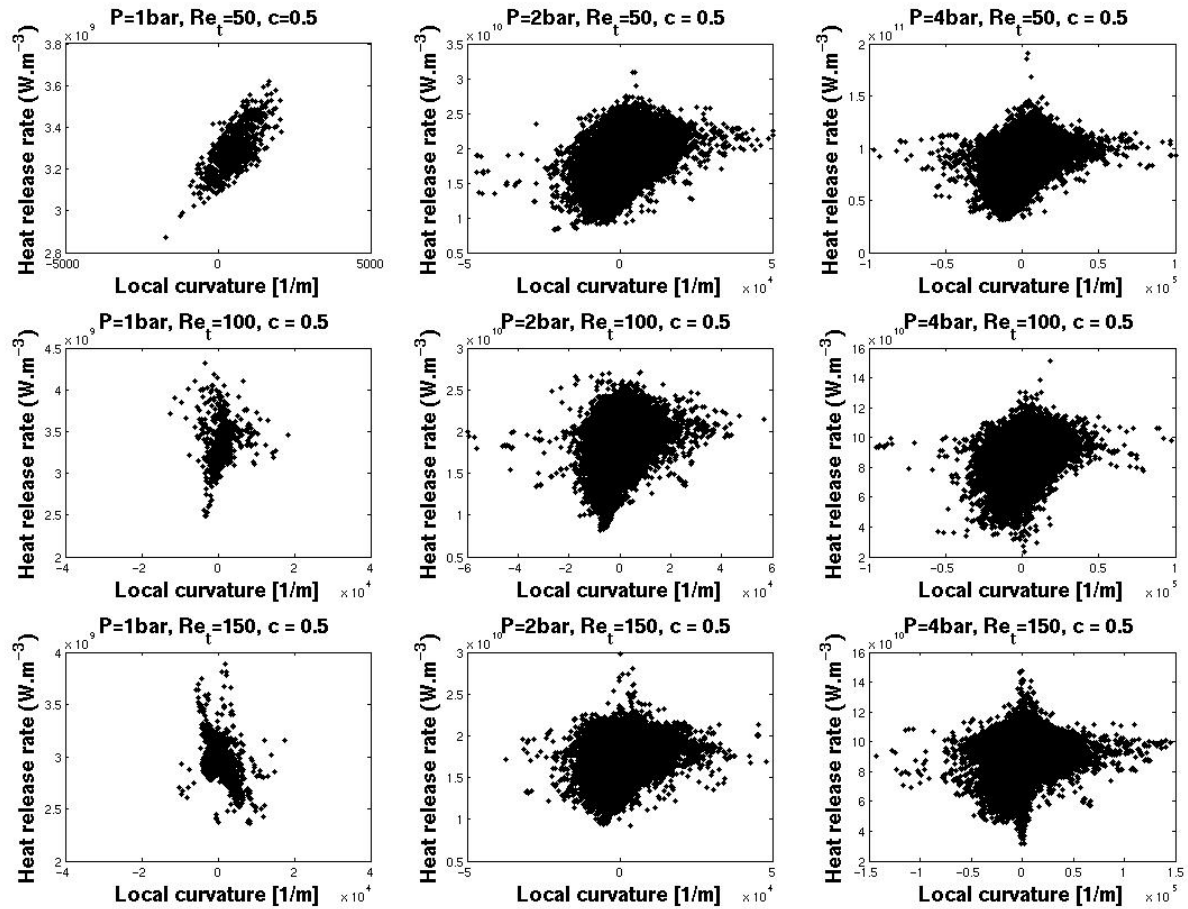


Fig.8. Scatterplots of heat release rate versus curvature at flame front for three pressure values varying from $p=1\text{bar}$ to 4bar at identical Re_t (left to right), and three turbulent Reynolds numbers varying from $Re_t=50$ to 150 at identical pressure (top to bottom).

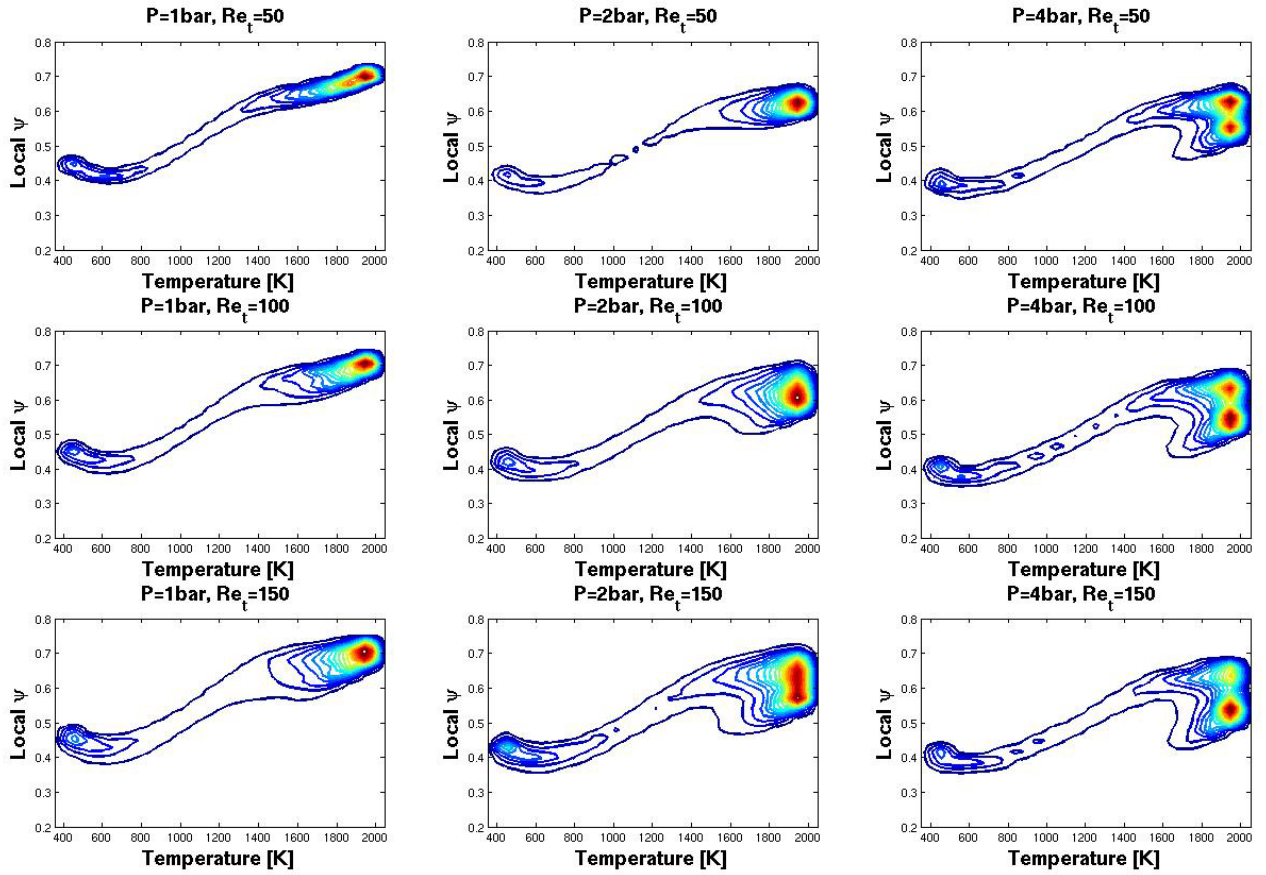


Fig. 9. Joint probability density function of hydrogen-to-oxygen mass ratio as a function of temperature for three pressure values varying from $p=1\text{bar}$ to 4bar at identical Re_t (left to right), and three turbulent Reynolds numbers varying from $Re_t=50$ to 150 at identical pressure (top to bottom).

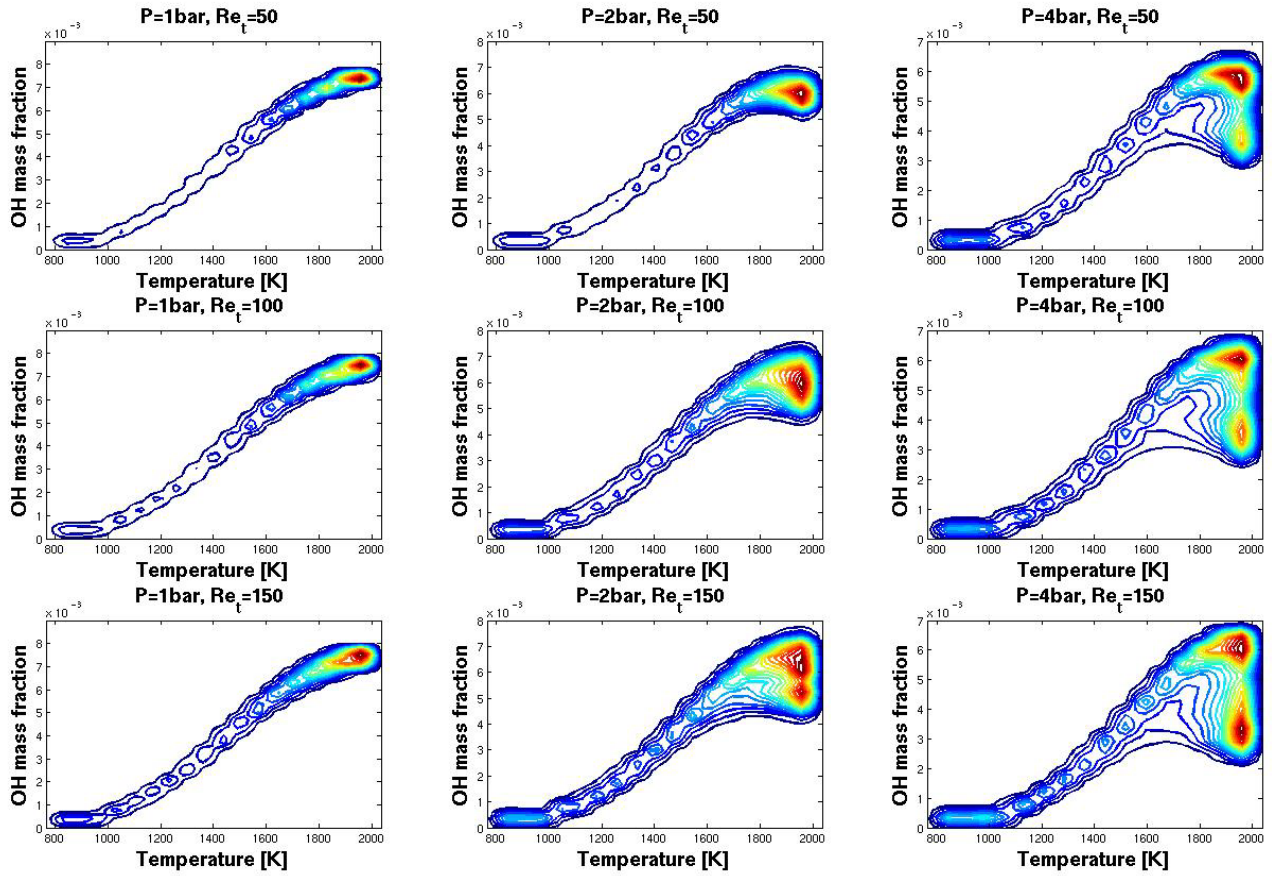


Fig. 10. Joint probability density function of mass fraction of OH as a function of temperature for three pressure values varying from $p=1\text{bar}$ to 4bar at identical Re_t (left to right), and three turbulent Reynolds numbers varying from $Re_t=50$ to 150 at identical pressure (top to bottom).

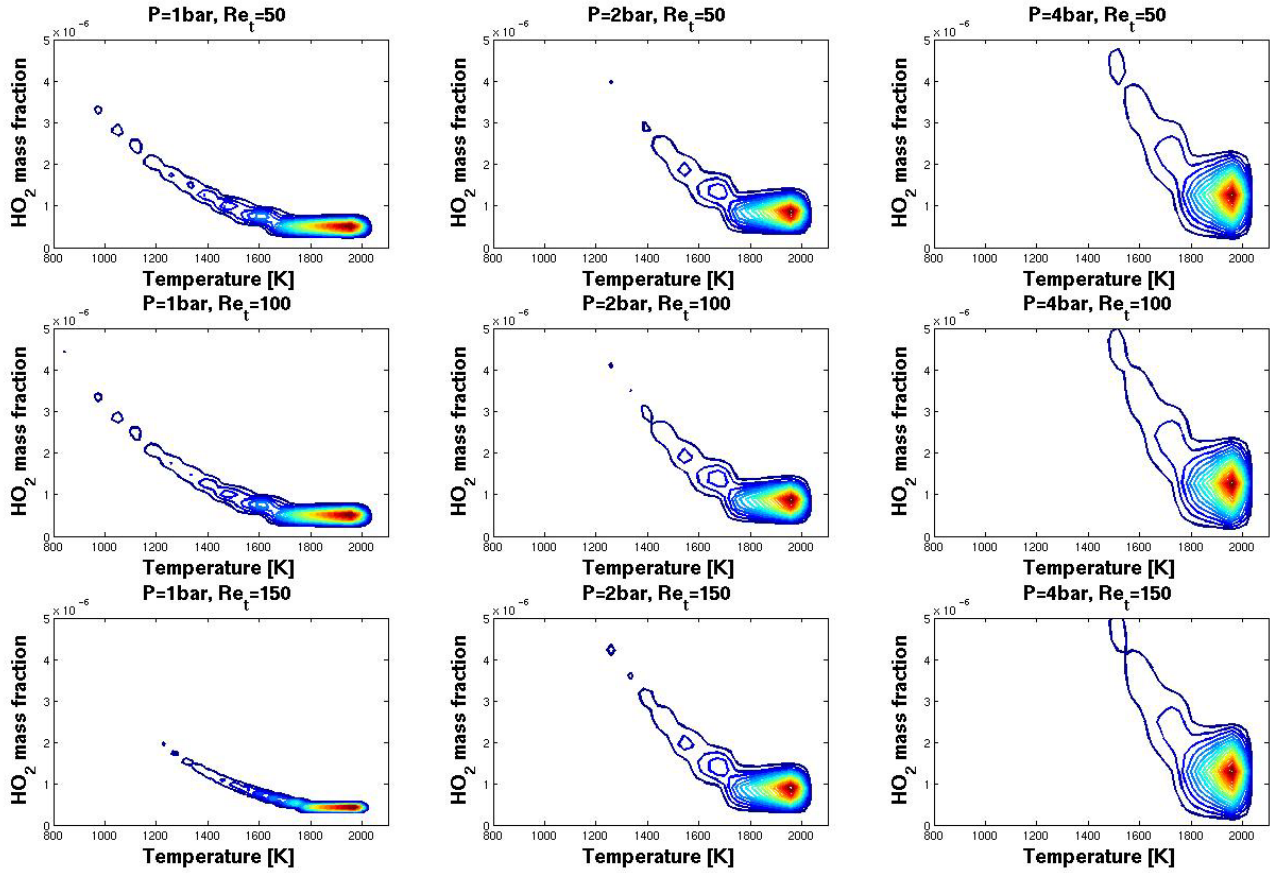


Fig. 11. Joint probability density function of mass fraction of HO₂ as a function of temperature for three pressure values varying from p=1bar to 4bar at identical Re_t (left to right), and three turbulent Reynolds numbers varying from Re_t=50 to 150 at identical pressure (top to bottom).

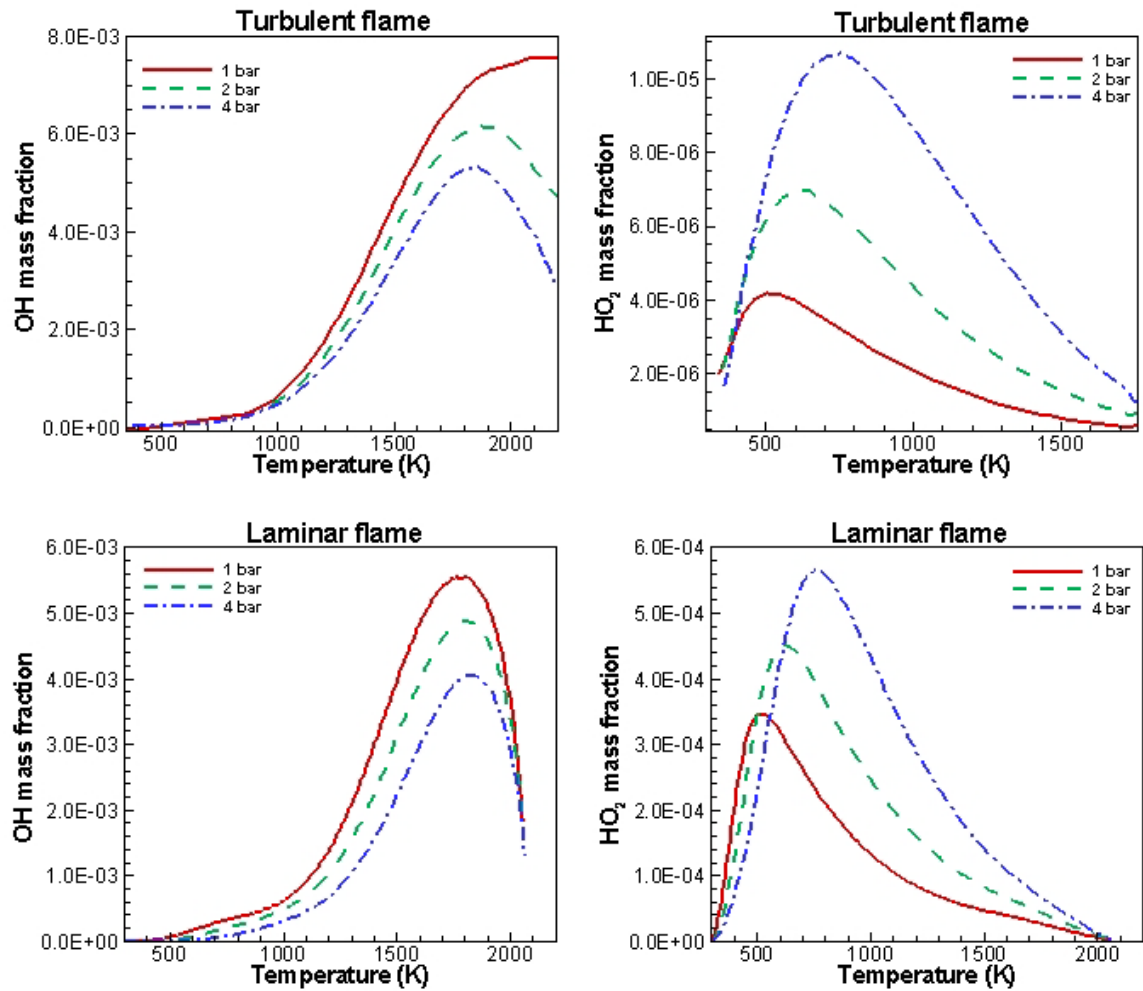


Fig. 12. Conditional mean values of mass fractions of OH and HO₂ radicals as a function of temperature for three pressure values of $p=1$ bar to 4 bar, (a) for turbulent flames with Reynolds number of $Re_t=150$ and, (b) for one-dimensional laminar flamelet.